

CHAPTER 5

Energy Applications of Bulk and Low Dimensional Topological Materials

This chapter focuses on multifunctional applications of bulk and low dimensional materials proposed in chapters 3 and 4. We begin with brief discussions on the background of the thermoelectric applications of bulk topological insulators and the implications of non-trivial topologies of binary zincblende AuI on the thermoelectric transport properties. We then discuss in brief the basal plane catalytic activity of low dimensional AuI towards hydrogen evolution reactions in terms of different mechanisms such as, volmer, volmer-tafel and volmer-heyrovsky. We then shift our focus on the edge sites rather than the basal plane of two dimensional topological insulators for catalytic applications. We establish a relation between the non-trivial topologies and catalysis. This is done by discussing topological quantum catalysis in two dimensional topological insulator LiMgAs.

5.1 Thermoelectric Applications of Bulk Topological Insulator: AuI

Zincblende phase of AuI binary compound was explored for non-trivial topological quantum phase transitions from semi-metallic to topological conducting/insulating phase. As expected, AuI binary compound did exhibit non-trivial topological properties which was discussed in

chapter 3. Apart from the non-trivial nature we were also motivated to explore the binary system AuI for thermoelectric applications. This is because, it was previously observed that, several strong topological insulators such as, Bi_2Te_3 , Bi_2Se_3 , Sb_2Te_3 host remarkable thermoelectric transport properties.¹ This implies that, materials hosting topological insulating nature can also exhibit decent thermoelectric properties due to linear band dispersions, dissipationless transport of Fermions, dense states across Fermi etc. Hence, till date, several bulk materials which exhibit non-trivial topological insulating nature also host thermoelectric phenomena.²⁻¹¹

As compared to other energy application materials, the field of thermoelectrics has been struggling due to the feeble power conversion efficiencies of conventional thermoelectric materials. Such drawback has restricted thermoelectric materials to niche applications such as, space probes, picnic refrigerators and domestic water heaters. Hence, the development of novel materials (which exhibit enhanced thermoelectric power conversion efficiencies) would promote the application of thermoelectric materials to harvest waste heat from major sources like thermal

stations/automobiles or replace conventional cooling techniques, eventually reducing the carbon footprints. The thermoelectric power conversion efficiency of a material can be quantified in terms of the figure of merit (defined as zT) which depends on, the seebeck co-efficient (S), electrical conductivity (σ), temperature, electronic thermal conductivity and, lattice thermal conductivity (κ). These parameters in turn depend on the carrier concentrations in a complex manner as evident from Fig. 5.1 which necessitates the optimization of carrier concentrations with respect to these parameters. From this Fig. 5.1 is evident that, alongwith carrier concentration, it is the overall optimization of zT which is important since other parameters exhibit significantly biased behaviour with respect to carrier concentrations. Hence, an ideal thermoelectric material can be realised in a sweet spot where, the zT is optimized which ensures efficient conversion of heat into electricity. Achieving such condition hence a non-trivial

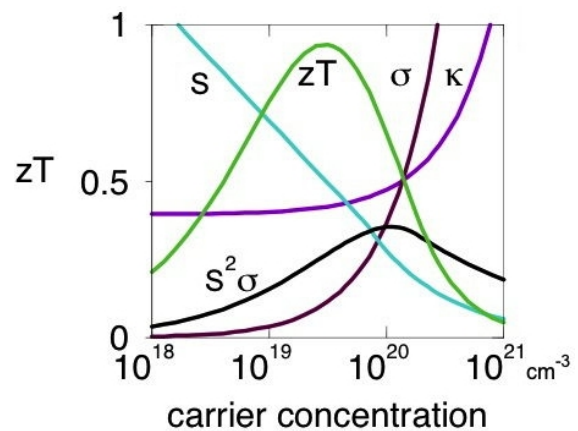


Figure 5.1: A typical schematic indicating the thermoelectric material design strategy with respect to carrier concentrations.

5. Energy Applications of Bulk and Low Dimensional Topological Materials

task requiring fine tuning of, the electronic band dispersion curves and the phonon dispersion curves. Hence, over the past few years, it has become a norm to, either tune the electronic transport of heavy materials (by band engineering, nano structuring, chemical doping, etc. which leads to lower thermal conductivity) or to suppress the thermal transport through lighter materials (by alloying, defects, dimensional confinement, etc.).¹²⁻¹⁸

However, the major hurdle which obstructs the thermoelectric efficiency arises due to an entanglement between, seebeck coefficient, electrical conductivity and thermal conductivity. This is due to the fact that these parameters are governed by the inter-dependent electrons and holes in a material. This leads to a compromised overall transport efficiency since, modification in one of the electronic parameters changes the other. Hence, the most effective method would be to minimize the lattice thermal conductivity by modifying the phonon transport properties of a material. Semi-metallic systems were known to host promising thermoelectric properties due to unconventional band topologies and coupled optical-acoustic phonon modes. However, such materials have received scare attention for thermoelectric applications.¹⁹⁻²² Recently, semi-metallic systems such as HgTe, BiTe etc. were investigated for thermoelectric applications.^{11,23-27} This motivates us to perform in-depth computations of the thermoelectric and transport properties of zincblende AuI apart from non-trivial topological quantum phase transitions.

Structure and Lattice Dynamics

As discussed in previous chapter 3, the zincblende phase of AuI is energetically, mechanically and dynamically stable. Apart from dynamic stability, observing phonon dispersion curves in the entire brillouin zone gives insights into, electron-phonon coupling (in metals), LO-TO splitting (in polar materials), flexural phonon modes (in two dimensional materials) etc. In case of zincblende AuI which is governed by the cubic symmetry we observe a narrow gap between acoustic and optic phonon branches. Such narrow gaps are known to reduce the thermal conductivity owing to the strong coupling between acoustic and optical branches.²⁸ Also, the highest observed phonon frequency was $\sim 110 \text{ cm}^{-1}$ along the brillouin zone path of $\Gamma \rightarrow X$ which was lower than some of the famous thermoelectric materials such as, Bi_2Te_3 , PbTe , SnSe and semi-metals such as, BiTe and HgTe .^{24,29-32} Contrary to these materials (wherein the highest optic mode is located at the centre of the brillouin zone) we observe a significant softening of the optical phonon modes and hardening of the acoustic phonon

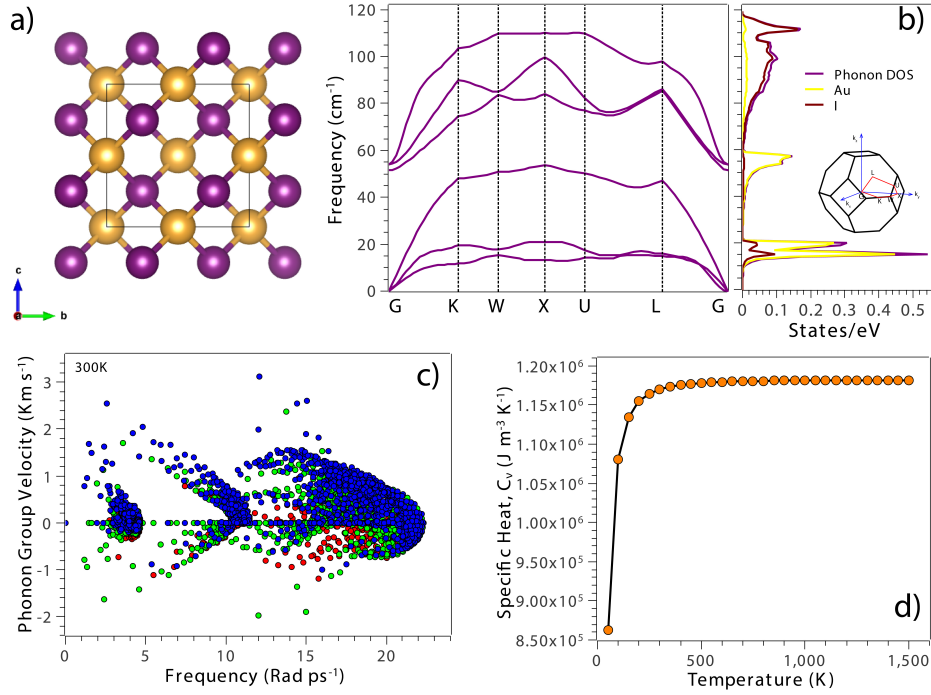


Figure 5.2: (a) Face centred cubic zincblende structure of AuI. (b) Phonon dispersion curves alongside phonon density of states. (c) Phonon group velocities versus frequency (rad ps⁻¹) and, (d) Specific heat (C_v) of AuI versus temperature.

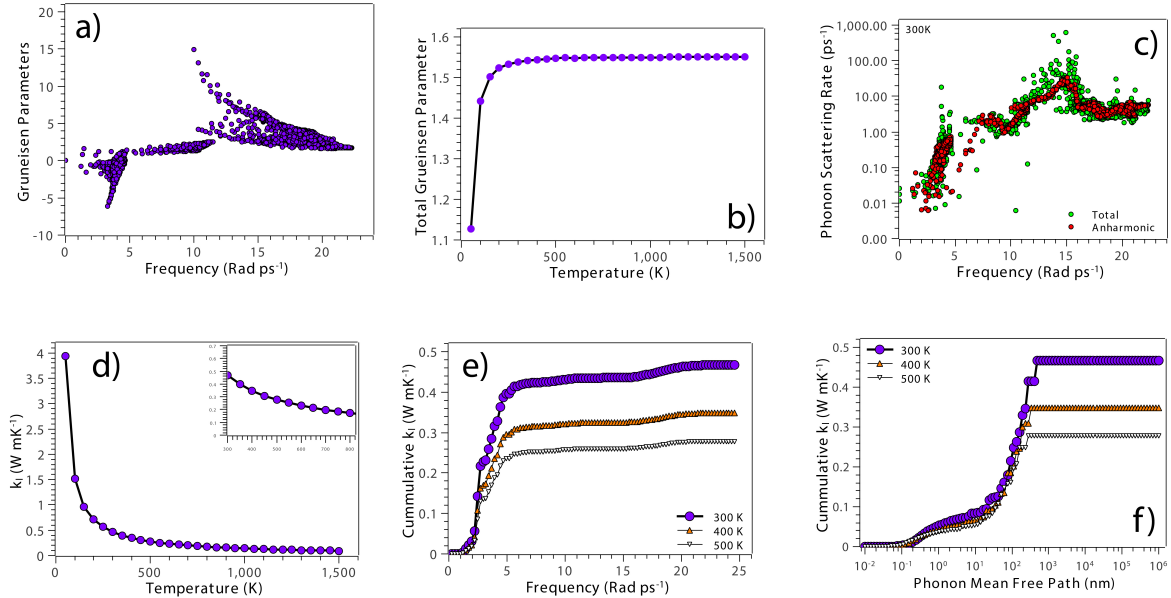


Figure 5.3: (a) Mode Grüneisen parameter as a function of phonon frequency. (b) Total Grüneisen parameters as a function of temperature. (c) Phonon scattering rates. (d) Lattice thermal conductivity and cumulative thermal conductivity as a function of, (e) Phonon frequency and (f) Phonon mean free path.

modes at the centre of the Brillouin zone. Such phonon dispersions are also observed in other compounds such as Perovskites and magnesium boride (MgB₂).^{33,34} Apart from this, the longitudinal acoustic mode has a frequency of $\sim 52 \text{ cm}^{-1}$ which is significantly lower than

the materials exhibiting low thermal conductivity. Phonon dispersion curves are of great significance when we intend to analyse the phonon group velocities (presented in Fig. 5.2(c)) which govern the transport properties. Generally, 90% of lattice thermal transport originates from the acoustic branches; however, recent reports suggest that, mild contributions may originate from the optical branches as well.^{35–39} Using phonon group velocities, we can project phonon number density on the phonon frequencies to understand the contributions arising from the acoustic and optical branches. Figure. 5.2(c) indicates that, apart from the acoustic branches, optical branches also contribute significantly. Also, the ultra-low optical phonon frequencies at the brillouin zone center reaffirm strong optic-acoustic coupling. Finally, in order to validate that AuI obeys the Dulong-Petit law, we compute temperature dependent specific heat (presented in Fig. 5.2(d)).

Thermoelectric Transport Properties: Lattice Contribution

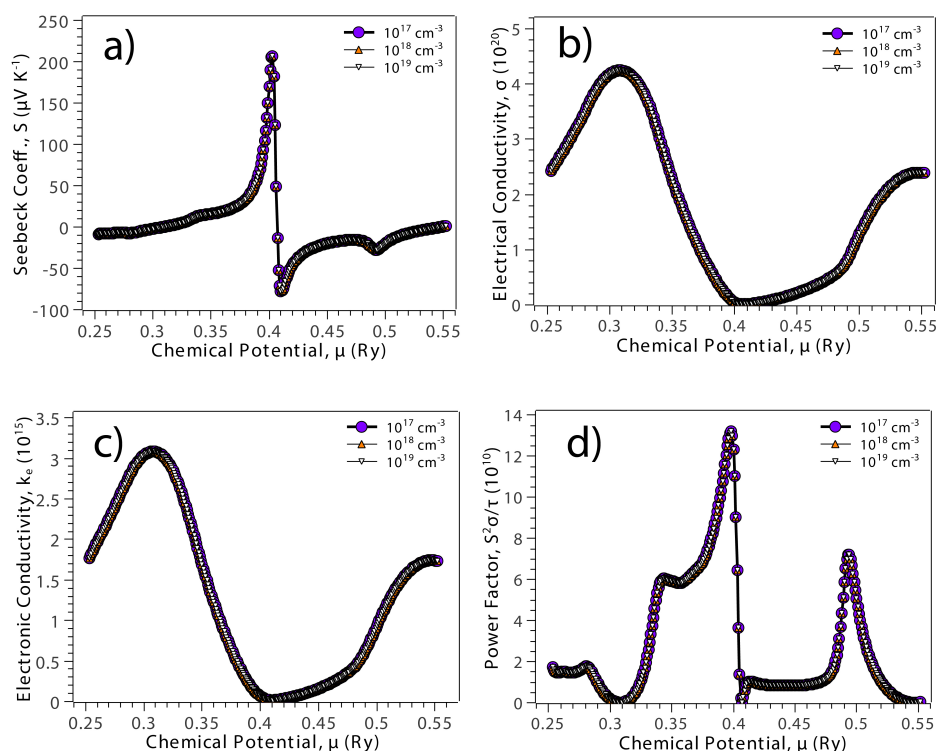


Figure 5.4: Electronic contribution to thermoelectric properties as a function of chemical potential (μ) for three different carrier concentrations.

We compute the electronic and lattice contributions to thermoelectric transport properties using the semi-classical Boltzmann transport equations for electrons and phonons. Firstly, we explore the role of lattice vibrations in terms of phonons on thermoelectric transport

properties. In Fig. 5.3(a) we present the mode Grüneisen parameters (γ) as a function of phonon frequencies. With this parameter, we get insights into the anharmonic effects originating from phonon-phonon interactions. This is done by computing the variations in the frequency of a phonon mode for a particular unit cell volume. From Fig. 5.3 it is clear that, Grüneisen parameters are widely spread indicating towards large anharmonic effects due to strong phonon-phonon scattering. Also, we observe suppression in phonon lifetimes and thermal conductivity which is due to enhanced anharmonicity. This is also clear from the Slack model which states that, the lattice thermal conductivity has inverse relation with the Grüneisen parameter.⁴⁰ This explains the large magnitudes of Grüneisen parameters and corresponding reduction in lattice thermal conductivity. In Fig. 5.3(b) we present the average magnitudes of Grüneisen parameters as a function of temperature. It is evident that, the magnitude of Grüneisen parameter saturates becoming almost constant (~ 1.55) at higher temperatures. This indicates that the crystal structure hosts strong bonding character. However, the computed magnitude of Grüneisen parameter is lower than other thermoelectric materials which implies lower anharmonicity as compared to, PbS (2.46), PbSe (2.66) and SnSe (2.83).³¹ The strong crystal bonding is also evident from the analysis of electro-negativity and charge distributions which indicate towards the polar-covalent bonding in the crystal. Also, the moderate magnitudes of young's and shear modulus indicate towards softening of bond strength which gives rise to reduced phonon transport.⁴¹

In Fig. 5.3(c) we present the phonon scattering rates for AuI which is explicitly used to interpret phonon lifetimes. These scattering rates are computed as a function of phonon frequencies in two scenarios wherein we, include and exclude the isotopic contributions arising from the mass anharmonicity. It was observed that, the overall phonon scattering rates follow the trend observed in the anharmonic scattering rates with slightly higher magnitude. This implies that, zincblende AuI exhibits mass anisotropy with isotropic effects contributing to the prediction of thermal transport properties. It is also evident from the literature that, the mass anisotropy is detrimental in predicting lattice thermal conductivity.⁴² Hence, to understand the effect of temperature we compute the scattering rates at higher temperatures. We found that, at higher temperatures, anharmonic effects dominate over the mass anisotropy. The temperature dependent thermal conductivity, cumulative magnitude of thermal conductivity as a function of phonon frequency and phonon mean free path are presented in Fig. 5.3(d), (e) and (f) respectively. It is evident that, the phonon mean free path decreases rapidly from 101

5. Energy Applications of Bulk and Low Dimensional Topological Materials

nm to 60 nm in the temperature range of 300-500 K. The magnitude of thermal conductivity at 300 K is 0.46 W/mK which is isotropic owing to the cubic symmetry of AuI. This value at room temperature is significantly lower than other materials such as, PbTe (2.2 W/mK), BiCuSeO (0.89 W/mK), HgTe (2.14 W/mK) and SnSe (0.6 W/mK).^{30–32,43}

One of the important factors in quantifying thermal transport properties is phonon lifetime which can be understood in terms of phonon scattering rates which in turn give rise to lower thermal conductivity. It is evident from the cumulative magnitudes of thermal conductivity (in terms of phonon frequency and mean free path) that, at a particular temperature, the thermal transportation by phonons leads to thermal conductivity. It is evident from Fig. 5.3(f) that, the characteristic mean free path at room temperature is 101 nm which reduces drastically to 76 nm and 60 nm at temperature of 400 K and 500 K respectively. This implies that, the average distance traversed by phonons (between two successive scattering events) decreases as the temperature increases. Hence, the overall thermal conductivity is suppressed.

Thermoelectric Transport Properties: Electronic Contribution

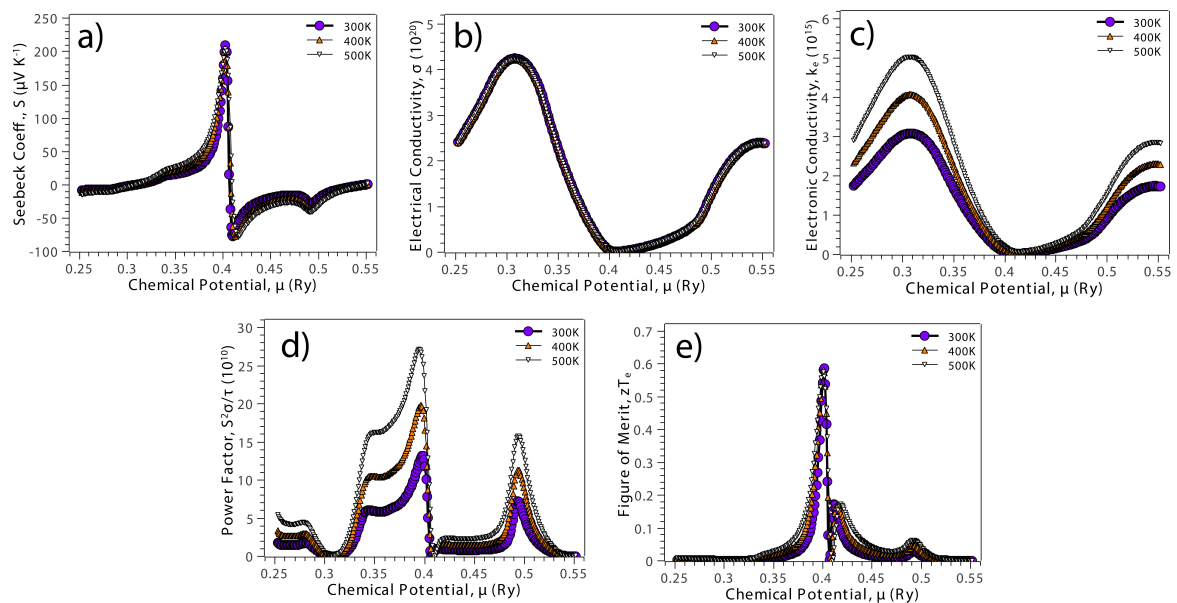


Figure 5.5: Computed electronic contributions to thermoelectric parameters as a function of chemical potential (μ) at three different temperatures.

Before we proceed with discussions regarding temperature dependent variations of electronic thermoelectric parameters, we address their variations as a function of the chemical potential for different carrier concentrations (as presented in Fig. 5.4). All the thermoelectric parameters exhibit converged behaviour at three different carrier concentrations (as evident

from Fig. 5.4). We observe that, the power factor is optimal at $1 \times 10^{19} \text{ cm}^{-3}$ carrier concentration. Hence, we proceed with computation of temperature dependent electronic thermoelectric parameters at this concentration. It is evident from Fig. 5.5 that, the electronic thermoelectric parameters for a fixed carrier concentration exhibit enhanced behaviour. This system exhibits promising power conversion efficiencies near room temperature due to the rise in power factor and the figure of merit (zT_e independent of the lattice thermal conductivity) which is evident from Fig. 5.5(d,e) in the temperature range of 300-500 K.

We compute temperature dependent relaxation time to compensate for the relaxation time dependent quantities (electrical and electronic conductivities) obtained using the semi-classical Boltzmann transport approach which would result in accurate magnitudes of electrical and electronic conductivities. Although, AuI exhibits unique electronic band topologies but the constituent charge carriers exhibit significantly distinct magnitudes of carrier mobilities. Here, enhanced electron mobility originates due to the inverse relationship between carrier effective mass and mobility. We observed that, the magnitude of electron mobility at room temperature was $58,930 \text{ cm}^2/\text{Vs}$ which is higher than the hole mobility $4,741 \text{ cm}^2/\text{Vs}$. Hence, we expect a reduced relaxation time for holes as compared to electrons. Here, the carrier relaxation time at room temperature were observed to be 1.8 ps and 0.67 ps for electrons and holes respectively.

Thermoelectric Transport Properties: Figure of Merit

We present the temperature dependent carrier mobilities, relaxation time, electrical and electronic conductivities independent of relaxation time in Fig. 5.6. In regime independent of relaxation time, the magnitude of power factor are affected drastically (as presented in Fig. 5.6(d) and (i)). The hole power factor was observed to be as low as $0.08 \text{ (V}^2/\text{K}^2\Omega\text{m)}$ (which even lower than the electron power factor of $0.22 \text{ (V}^2/\text{K}^2\Omega\text{m)}$) due to low hole mobility and relaxation time. The Seebeck co-efficient for hole and electron were observed to be comparable with magnitudes ranging as $150\text{-}200 \mu\text{V/K}$ at 300-600 K temperature (as evident from Fig. 5.6(a) and (f)). Also, we observed a significant difference in the room temperature electronic and electrical conductivities (as evident from Fig. 5.6 (b)-(c) and (g)-(h)). With such mutually compensating characteristics (i.e., similar thermal conductivities and Seebeck coefficient with negligible difference as evident from Fig. 5.6(a) and (f)), the overall figure of merit (zT) turns out have similar character in case of holes and electrons. The nature of overall zT exhibits an inverted parabolic trend (as evident from Fig. 5.6(e) and (j)), with a

5. Energy Applications of Bulk and Low Dimensional Topological Materials

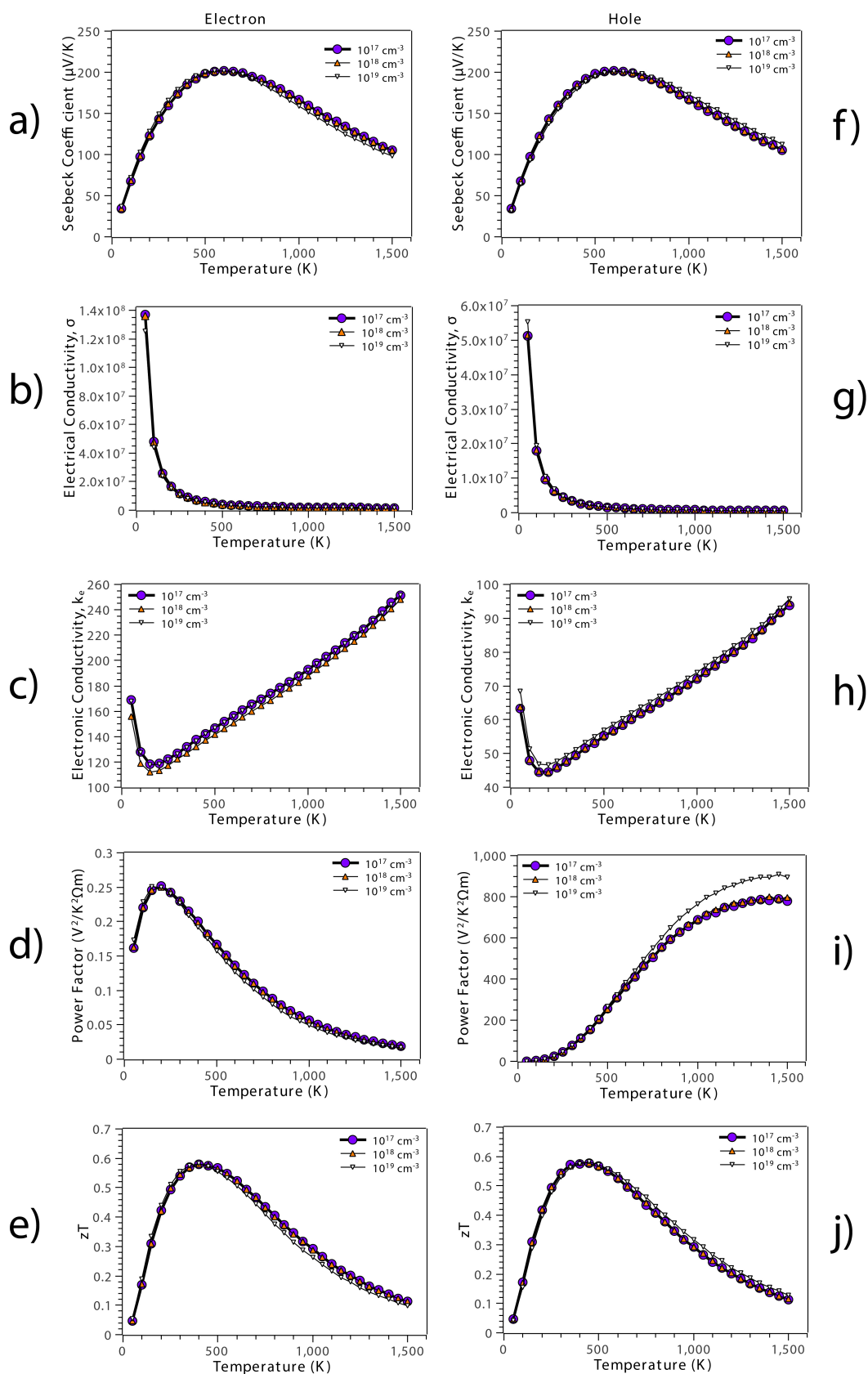


Figure 5.6: Variation of thermoelectric parameters and total Figure of Merit for three different carrier concentrations.

maximum magnitude of 0.58 and 0.57 observed at 400 K for electrons and holes respectively. Such room temperature figure of merit is quite remarkable as compared to several materials which exhibit high figure of merit at higher temperatures. This figure of merit can be further enhanced to realise efficient thermoelectric power conversion by optimizing the power factor. This can be achieved through chemical doping or dimensional engineering which modulates the electronic band structure.

Hence, topological insulators can be realised to be efficient thermoelectric materials. However, it would be interesting to explore topological insulators for other energy applications such as electro-catalysis. With this motivation we explored two dimensional AuI which was dimensionally engineered from the bulk parent and observed to exhibit non-trivial topology in chapter 4. Eventually, we observed that, the basal activity of two dimensional topological insulators (such as AuI) is decent but not excellent. This lead us to explore the most recently developed field of topological quantum catalysis in low dimensional systems. This phenomena was explored in two dimensional LiMgAs which exhibits non-trivial topological properties.

5.2 Catalytic Activity of Two Dimensional Topological Insulator: AuI

Two dimensional phase of AuI was explored in chapter 4 for non-trivial topological insulating nature. Further to these investigations, we also explored AuI monolayers for catalytic activity. This was out of curiosity (i.e., how would AuI monolayer respond towards hydrogen evolution reaction?) since, Au is one of the precious transition metals known for catalytic applications. With this we hope to propose a two dimensional material which can be used as a catalyst to facilitate energy conversions sufficing the rising energy demands. The motivation lies in several low dimensional materials which were previously explored for catalytic applications and discussed in following paragraphs.

Metal halides have recently received attention for potential applications such as, photo-catalysts, ultraviolet optical devices and quantum cutting solar materials.⁴⁴ For example, Huang et.al., recently investigated binary compounds comprising of group-11 transition-metals and halides.⁴⁴ It was proposed by Huang et.al., that such binary compounds can be mechanically exfoliated from their bulk counterparts. Also, alloy monolayers of Cu, Ag, Au and Pt were explored for nano- and opto-electronic applications.⁴⁵ This was possible

5. Energy Applications of Bulk and Low Dimensional Topological Materials

due to various Au based nanostructures (such as, nano-particles, nano-wires, nano-ribbons, nano-plates, nano-sheets and nano-tubes) which can be synthesized experimentally.⁴⁶⁻⁵¹

From perspective of a catalytic material, to efficiently achieve hydrogen evolution reaction Au based materials have turned out to be potential alternatives as compared to rare metals such as platinum (Pt), palladium (Pd) etc.⁵²⁻⁵⁴ The standard catalytic materials of choice explored thus far are typically made up of, Pt, Pd and their alloys. These materials host spontaneous hydrogen evolution reactions with Gibbs free energy close to zero.^{55,56} This criteria has inspired exploration of numerous two dimensional transition metal based catalysts for hydrogen evolution reaction.⁵⁷⁻⁶¹ Apart from the transition metal based compounds, the material search has proliferated into single atom catalysis which employs single atoms of precious metals such as Pt, Pd, Au etc. Tran et.al., have shown that, the reaction Gibbs free energy can be further reduced by designing catalysts made up of MoS₂ and Mo₃S₁₃ with Au substrate.⁶²⁻⁶⁵ Similarly, Au nano-particles were also explored as catalyst for hydrogen evolution reaction. It was observed that, nano-particles provide best alternative for Pt free catalysis owing to their large surface area as compared to the volume occupying the space. Apart from this, Au based catalysts exhibit good activity for water-gas shift reactions at low temperatures as compared to Pt catalyst.⁵² Also, NiAu/Au core shell's and materials with Au at corner sites; were found to exhibit promising catalytic activity as compared to Pt based catalyst with the latter being more active for hydrogen evolution reaction as compared to CO₂ reduction.^{66,67}

Catalysis Mechanism

We explored the catalytic activity of AuI monolayer at 0% strain since this structure was found to be thermodynamic stability with a narrow electronic band gap. We might expect that, under pristine conditions, AuI monolayer (which exhibits non-trivial topological properties) would facilitate catalytic activity along the edges due to the non-trivial edge charge accumulation.⁶⁸ But, since the non-trivial gap (~ 14.4 meV) was found to be smaller than thermal energy at room temperature (~ 25 meV) the resulting charge accumulation along the edges won't be high enough to facilitate catalytic activity as compared to the basal plane. Hence, we investigated the catalytic activity along the basal plane of pristine AuI monolayer.

A typical hydrogen evolution reaction is a multi-step process as presented in Fig. 5.7(a). Typically, the hydrogen evolution reaction begins with the interaction and adsorption of a

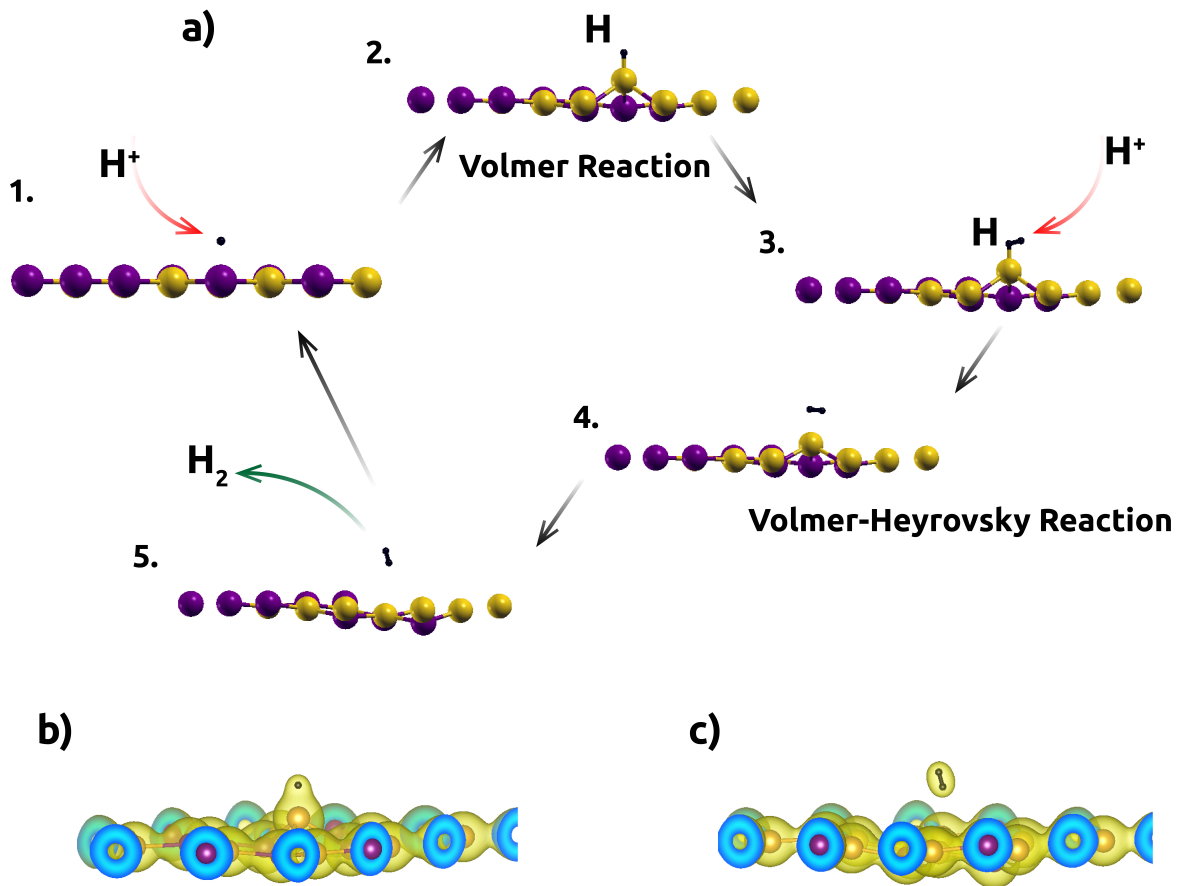


Figure 5.7: (a) Steps involved in the catalysis mechanism of AuI monolayer in hydrogen evolution reaction. Charge density plot of (b) Volmer and (c) Volmer-Heyrovsky reactions.

primary hydrogen over the catalyst surface (as presented in Fig.5.7(a)). This is known as the Volmer reaction (as evident from step 1. in Fig. 5.7(a)). Every catalyst should obey Sabatier's principle which states that, the intermediate state in a chemical reaction is characterised by optimal binding of the adsorbate and the adsorbant. Hence, in a hydrogen evolution reactions the primary hydrogen should form optimal bond with the catalyst surface (neither too weak nor too strong) facilitating the Volmer reaction. This would ensure the formation of a hydrogen molecule due to the interaction of primary hydrogen with the secondary hydrogen.

Such reaction mechanism is quantified in terms of, optimal adsorption energy ($\Delta E_H = 0.24$ eV) and Gibbs free energy ($\Delta G_H = 0.00$ eV) during the Volmer reaction under $pH = 0$ and for a reduction potential of $U = 0$. These parameters have attained the reputation of reliable descriptors for hydrogen evolution reaction. These parameters i.e., the adsorption energy and the Gibbs free energy are computed as, $\Delta G_H = \Delta E_H + \Delta_{ZPE} - T\Delta S$ and $\Delta E_H = (E_{AuI+H} - E_{AuI} - \frac{1}{2}E_{H_2})$ respectively. Here, ΔE_H presents the hydrogen adsorption energy, Δ_{ZPE} presents the zero-point energy between the adsorbed and gaseous phases of

5. Energy Applications of Bulk and Low Dimensional Topological Materials

hydrogen atom and ΔS is the change in entropy between the adsorbed and gaseous phases of hydrogen atom. Generally, the term $\Delta_{ZPE} - T\Delta S$ is approximated to be 0.24 eV. In case of an ideal catalyst for hydrogen evolution reaction, ΔG_H should be zero. Hence, we typically expect optimal adsorption energy value of $\Delta E_H = -0.24$ eV during the Volmer reactions. The terms E_{AuI+H} and E_{AuI} are the total energies of hydrogen adsorption on, top sites (i.e., on top of Au/I, bridge and hollow) and total energy of pristine AuI respectively. E_{H_2} is the total energy of H_2 molecule in vacuum. We employ these equations to compute the adsorption energies along the four sites (i.e., top of Au/I, bridge and hollow) of a $3 \times 3 \times 1$ AuI monolayer.

From our computations we found that, top of Au was the most favourable site for primary reaction with adsorption energy (-0.64 eV) and the Gibbs free energy (-0.40 eV) close to optimum values. Similarly, the Gibbs free energy at I, bridge and hollow sites are 0.90 eV, -1.25 eV and -0.49 eV respectively. From the analysis of the Lowdin charge we found that, a charge transfer of $\sim 0.26e$ occurs from Au site to the primary hydrogen (as evident from step 2. in Fig. 5.7(a) and (b)). The charge redistribution is such that, the charge over Au gets depleted while charge over I gets accumulated.

Following the primary reaction, the hydrogen evolution can occur through two different mechanisms such as, Volmer-Tafel and Volmer-Heyrovsky. In a Volmer-Tafel reaction the primary hydrogen reacts with a secondary hydrogen adsorbed on a neighbouring site leading to the evolution reaction. But in case of AuI, on adsorption of a secondary hydrogen over I site (which is the nearest neighbour to Au site where the primary hydrogen is adsorbed) we observe a high charge transfer as compared to that at Au site i.e., $\sim 0.43e$. The corresponding Gibbs free energy also indicates towards a strong interaction of the secondary hydrogen at I site. Hence, AuI monolayer won't facilitate Volmer-Tafel reaction owing to the strong interactions at I site. Even the Volmer-Tafel reaction at a neighbouring Au atom won't be possible since, the distance between the two such Au atoms would be quite large (~ 4.7 Å). However, in practical conditions, the primary hydrogen might interact with a secondary hydrogen originating from the surroundings (as evident from step 3-5 presented in Fig. 5.7(a)). Such reaction mechanism is known as Volmer-Heyrovsky reaction.

The adsorption energy of a secondary hydrogen during a Volmer-Heyrovsky reaction is given as, $\Delta E_{H^*} = \frac{1}{n}(E_{AuI+nH^*} - E_{AuI} - \frac{n}{2}E_{H_2})$ and the corresponding Gibbs free energy is given as, $\Delta G_{H^*}(n) = \Delta E_{H^*}(n) + \Delta_{ZPE} - T\Delta S$. We proceed with the adsorption energy and Gibbs free energy formalisms proposed by Lee et.al., for Volmer-Tafel reactions. We found

that, the Gibbs free energy for Volmer-Tafel reaction was -0.62 eV which was higher than that for Volmer-Heyrovsky -0.23 eV. This indicates that, the most favourable mechanism for hydrogen evolution reaction is Volmer-Heyrovsky (at Au site as presented in Fig. 5.7(a)) rather than Volmer-Tafel. Hence, AuI monolayer would facilitate the evolution of hydrogen molecule through Volmer-Heyrovsky mechanism (as evident from Fig. 5.7(a-c)).^{69,70}

Therefore, we can ask a question; in low dimensional topological materials such as, two dimensional topological insulators can we expect superior catalytic activity as compared to the one observed in the basal planes of AuI? Will the large non-trivial spin-orbit interactions induced gap would facilitate such behaviour? For this purpose, we explore a completely new phenomena which is currently at the frontiers of materials science research and known as topological quantum catalysis. For this purpose, we choose two dimensional topological insulator LiMgAs (explored in chapter 4) which exhibits large non-trivial gap, leading to large edge charge accumulations.

5.3 Topological Quantum Catalysis in LiMgAs

Why exactly do we need a topological quantum catalyst? The need arises due to the rise in global energy demands which has attained great importance over the past few decades.⁷¹⁻⁷³ To address the rise in global demand, the primary focus was on generation of energy using Hydrogen-rich resources. This technique was observed to be effective which lead to the use of Platinum group metals such as, Pt, Ru, Rh, Ir and Pd as a catalysts in hydrogen evolution reactions.⁷⁴ But, just as any promising material, these rare metals came with a disadvantage of; associated cost, rarity and short lifetime of electrodes. This has motivated extensive research in materials science to find a cost-effective and abundant alternative. Thus far, combination of metals (such as, Pt, Pd, Ir, Ru, Au, Ni), binary metal alloys, 3d transition metal hydroxides, phosphides, carbides and transition metal chalcogenides, nitrides, borides, oxides and sulphides were proposed as promising; cost-effective alternatives.^{74,75} But, the efficiency and performance of such materials depended on the pH of surrounding media leading; different results in acidic and alkaline media.⁷⁵

In a catalytic reaction, the major factor governing the activity, efficiency and performance originates from the surface states. These surface states in turn originate from; [111] surfaces of noble metals and the surface dangling bonds of a semi-conductor which significantly affect

5. Energy Applications of Bulk and Low Dimensional Topological Materials

the physio-chemical processes occurring at the interfaces and surfaces.⁷⁶ These surface states arise due to the spatial proximity and orbital features across the Fermi level. Although these surface states are promising but, they are typically quite sensitive and not robust against, impurities in crystal lattice, defects and surface degradation (due to redox reactions) which are known to alter the atomic terminations and crystal orientations.⁷⁶ Also, as suggested by Gerischer and Parson, another major challenge faced by materials is that, they have to obey Sabatier's principle which talks about thermoneutral condition (yielding maximum exchange current densities).⁷⁷⁻⁸⁰ Hence, realising materials which simultaneously would host robust surface states to facilitate physio-chemical reactions and obey Sabatier's principle is quite a challenging task.

With the discovery and experimental realisation of topological quantum materials (such as, topological insulators and topological semi-metals (Dirac, Weyl, Nodal-line)) we can now address the problems with existing catalysts mentioned in previous paragraph.⁸¹ The characteristic features which makes these materials stand out from existing catalysts is that, the conducting surface/edge states and Fermi arcs are robust to crystal impurities (magnetic/non-magnetic) and surface oxidations/degradations. This implies that, the catalyst material would have longer life-times facilitating hydrogen evolution reaction due to the sea of electrons which exhibit high mobilities.⁸¹ This approach to solve the problem in catalysis was initially proposed in 2011 wherein, gold-covered surface of Bi₂Se₃ topological insulators were investigated for CO and O₂ adsorptions. It was observed in this initial work that the surface states persisted as long as the bulk gap was retained under time-reversal symmetry.⁷⁶ The results were quite promising with the potential of being implemented as alternatives to conventional *d*-band heterogeneous catalysis. However, ever since then, the phenomena of topological quantum catalysis received scarce attention until recently; when a new perspective was proposed for heterogenous catalysis using materials such as, topological semi-metals, chiral crystals, Full/Half-Heusler alloys and Perovskite manganites.⁸²

However, the lower carrier densities across the Fermi level originating from the weak electrostatic screening strength is a major drawback of the topological semi-metals (such as, Dirac and Weyl semi-metals) making them less reliable.⁸³ We therefore revisit and investigate the potential role of conducting edge states of a two dimensional topological insulator in heterogenous catalysis. This is because, topological insulators exhibit, high carrier mobilities, high carrier densities across Fermi level and robust charge accumulations along the

edges. We investigate the catalytic response of the edge states of two dimensional topological insulator LiMgAs along [100] and [010] crystal directions. We explicitly established the fact that, the catalytic response and performance gets significantly enhanced due to the edge states originating from the spin-orbit interactions. With this, we hope that, we can bypass conventional d -band theory and single atom catalysis with topological quantum catalysis for varied applications.

Structure and Lattice Dynamics

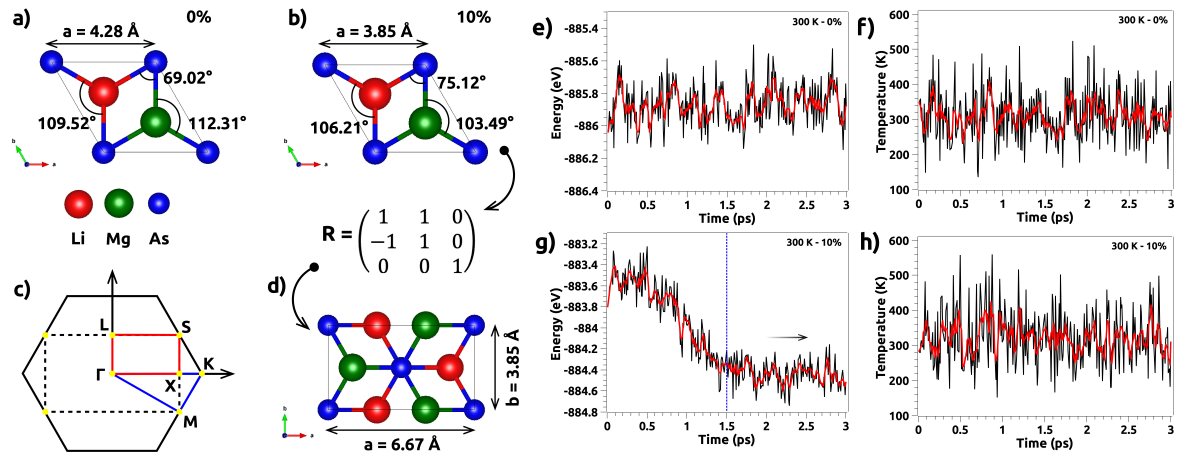


Figure 5.8: (a,b) Unit cell of LiMgAs at 0% strain and 10% biaxial compressive strain (corresponding monolayer thickness (h) is 1.60 \AA and 1.95 \AA respectively). (c) The hexagonal and orthorhombic Brillouin zone obtained using matrix (\mathcal{R}) (d). (e-h) ab-initio molecular dynamics simulations under 0% strain and 10% compressive strain for 3 picoseconds at 300 K.

We build upon the two dimensional topological insulator LiMgAs which has been discussed in chapter 4. At 0% strain, LiMgAs monolayer (governed by $\bar{P}3m1$ space group) exhibits structure similar to 1T-MoS₂ with, the hexagonal lattice of As atoms occupies octahedral coordinations between two layers of hexagonal-closed-packed structures made up of Li and Mg (as presented in Fig. 5.8(a)) with the octahedral belonging to D_{3d} tetragonal symmetry.⁸⁴ This structure is retained even at 10% biaxial compressive stress (i.e., after topological quantum phase transition) as evident from Fig. 5.8(b). The dynamic stability of LiMgAs was established in chapter 4, hence we investigated the stability and viability of LiMgAs at room temperature (300 K) by performing ab-initio molecular dynamics simulations. From Fig. 5.8(e-h) we observe that, the structure of LiMgAs at 0% and 10% biaxial compressive stress are stable due to small variations in the energy and thermostat temperature. However, under 10% biaxial

5. Energy Applications of Bulk and Low Dimensional Topological Materials

compressive stress we observe that, the system initially exhibits large fluctuations in energy (Fig. 5.8(g)) but eventually thermalise after 1.5 picoseconds (highlighted blue line in Fig. 5.8(g)) attaining structural stability.

With the stability established, we used a rotation matrix (\mathcal{R}) to transform the hexagonal unit cell into an orthorhombic unit cell at 10% biaxial compressive stress (presented in Fig. 5.8(b,d)). This phase was used to obtain, zig-zag and planar like nanoribbon configurations by exploiting periodicity along [100] and [010] crystal directions respectively. We investigated the energetic stability of these nanoribbon configurations (presented in Fig. 5.9(c,d)) in terms of the formation energy E_f ($= E_{\text{LiMgAs}} - E_{\text{Li}} - E_{\text{Mg}} - E_{\text{As}}$, where E_{LiMgAs} is the energy of LiMgAs and E_X ; $X = \text{Li, Mg, As}$; are the total energies of constituent elements) and found them to be -2.03 eV/atom and -2.90 eV/atom for zig-zag and planar like configurations respectively. This indicates that the nano-ribbon configurations are energetically lower as compared to their two dimensional monolayer which has formation energy -1.70 eV/atom. Hence, LiMgAs nanoribbons are energetically stable and viable experimentally.

A Revisit to Topological Properties

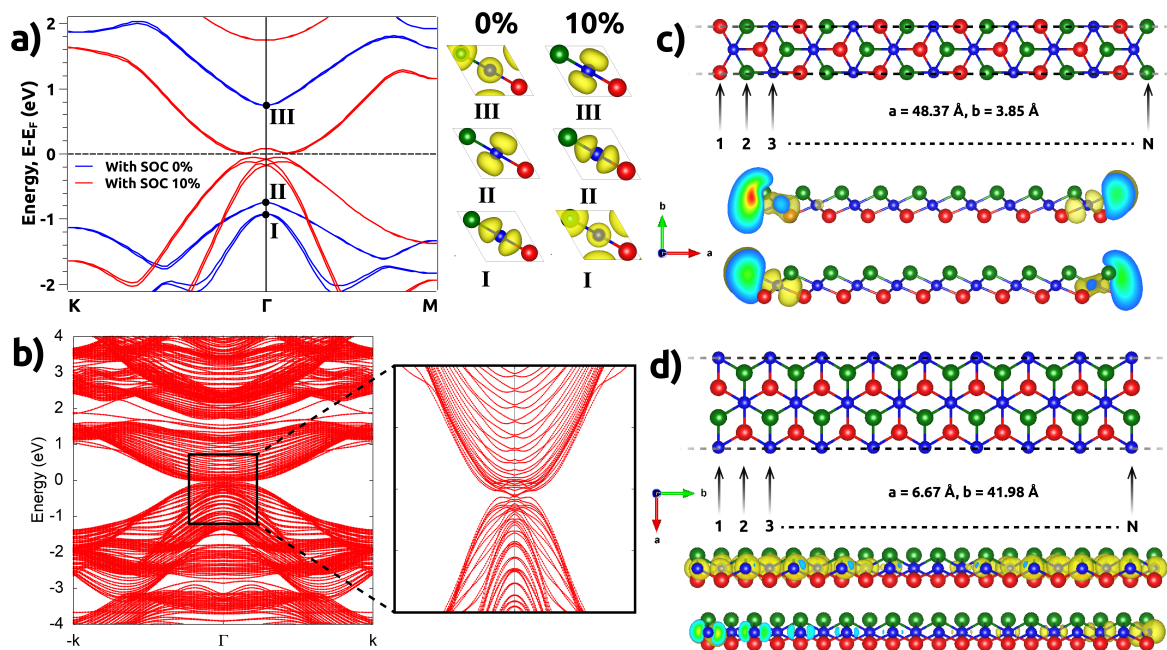


Figure 5.9: (a) Electronic band structure with spin-orbit interactions at 0% and 10% biaxial compressive strain alongside the charge densities of bands I, II and III. (b) Edge slab band structure. (c,d) Zig-zag and planar terminations of nanoribbons with lattice parameters.

Since, two dimensional LiMgAs is a non-trivial topological insulator which is realised

through topological quantum phase transitions, it exhibits edge charge accumulations which are robust against external perturbations. Apart from the s - p orbital inversion mechanism discussed in chapter 4, in Fig. 5.9(a) we present the electronic band structures of LiMgAs at 0% and 10% biaxial compressive stress under the influence of spin-orbit interactions. It is evident from Fig. 5.9(a) that, the charge densities get exchanged across the Fermi level (i.e., the charge densities of bands I, II and III at 0% and 10% biaxial compressive stress get exchanged); confirming the non-trivial nature of topological quantum phase transition. Upon quantum phase transition, in the non-trivial regime (at 10% stress) the system was observed to exhibit a large-gap of 0.16 eV which is superior to several materials.⁸⁵ This indicates that, the edge charge accumulations would persist at room temperature since the gap is quite high as compared to the thermal energy at room temperature. In chapter 4 we observed that, the non-trivial phase of LiMgAs hosts high velocity Fermions along the conducting edge states.

Hence, we can expect unconventional catalytic response of the edge sites of LiMgAs towards hydrogen evolution reaction. The conducting edge sites are evident from Fig. 5.9(b) which shows the slab band structure computed using the exact tight-binding Hamiltonian model. With this we confirmed that, the edge sites are semi-metallic while the bulk bands host a spin-orbit interactions induced gap at 10% biaxial compressive stress. These semi-metallic conducting edge sites can be visualised in terms of the edge charge accumulations. The charge density plots presented in Fig. 5.9(c,d) indicate towards Fermionic accumulations along the edge sites owing to the non-trivial topology. Therefore, we can exploit these non-trivial charge accumulations to host topological quantum catalysis along the edges as compared to basal sites.

Basal Catalytic Activity

We began our investigations with the basal sites and eventually established that, the edge sites are superior as compared to the basal sites. We began our computations with $3 \times 3 \times 1$ supercell of the two dimensional topological insulator LiMgAs which exposes the basal sites for hydrogen evolution reaction. The primary Volmer reaction was carried out at different sites such as, top (of Li, Mg, As) and bridge sites (such as, Li-Mg, Mg-As, Li-As). The primary reaction should obey Sabatier's principle which implies that, the interaction of primary hydrogen should be optimal. This is quantified in terms of, adsorption energy ($\Delta E_H^{ads} = E_{LiMgAs+H} - E_{LiMgAs} - \frac{1}{2}E_{H_2}$) where, $E_{LiMgAs+H}$ is the total energy of H adsorbed

5. Energy Applications of Bulk and Low Dimensional Topological Materials

LiMgAs, E_{LiMgAs} is the total energy of LiMgAs and E_{H_2} is the total energy of H_2 molecule) and Gibbs free energy ($\Delta G_H = \Delta E_H^{ads} + \Delta_{ZPE} - T\Delta S$ where, Δ_{ZPE} is the change in the zero-point energy of adsorbed and gaseous state of H and ΔS is the corresponding change in the entropy and T is room temperature) which should be -0.24 eV and 0.00 eV respectively, under neutral pH and reduction potential of $U = 0$.⁸⁶

Spin-orbit interaction	Site	E_H^{ads} (eV)	ΔG_H (eV)
OFF	Li	-3.430	-3.190
	Mg	-2.522	-2.282
	As	-2.380	-2.140
	Li-As	-3.838	-3.598
	Mg-As	-3.632	-3.392
	Li-Mg	-3.871	-3.631
ON	Li	-3.859	-3.619
	Mg	-2.601	-2.361
	As	-2.462	-2.222
	Li-As	-3.909	-3.669
	Mg-As	-4.084	-3.844
	Li-Mg	-4.325	-4.085

Table 5.1: Adsorption and Gibbs free energy at different basal sites of LiMgAs with and without spin-orbit interactions (SOI).

It was observed that, As top site was the most active sites during the primary reaction (amongst rest of the basal sites) with adsorption and Gibbs free energy without spin-orbit interactions (with spin-orbit interactions) as -2.38 eV (-2.46 eV) and -2.14 eV (-2.22 eV) respectively (the values for other sites are presented in Tab. 5.1). Due to the strong interactions on almost all the basal sites, we conclude that, the basal sites won't be ideal for catalytic application such as for hydrogen evolution reaction.

Topological Catalysis

As compared to the interactions on basal sites, the edge sites exhibit excellent activity during the primary reaction due to robust charge accumulations (presented in Fig. 5.9(c,d)). Different reaction mechanisms were investigated (in both zig-zag and planar termination configurations of nanoribbons 5.10(a,b)) to get insights into the hydrogen evolution reaction assisted by the robust edge states of the two dimensional topological insulator LiMgAs. The sites investigated for hydrogen evolution reaction were, top (Li, Mg, As) and bridge sites (Li-As, Mg-As). During the primary reaction, most active sites of zig-zag and planar configurations without

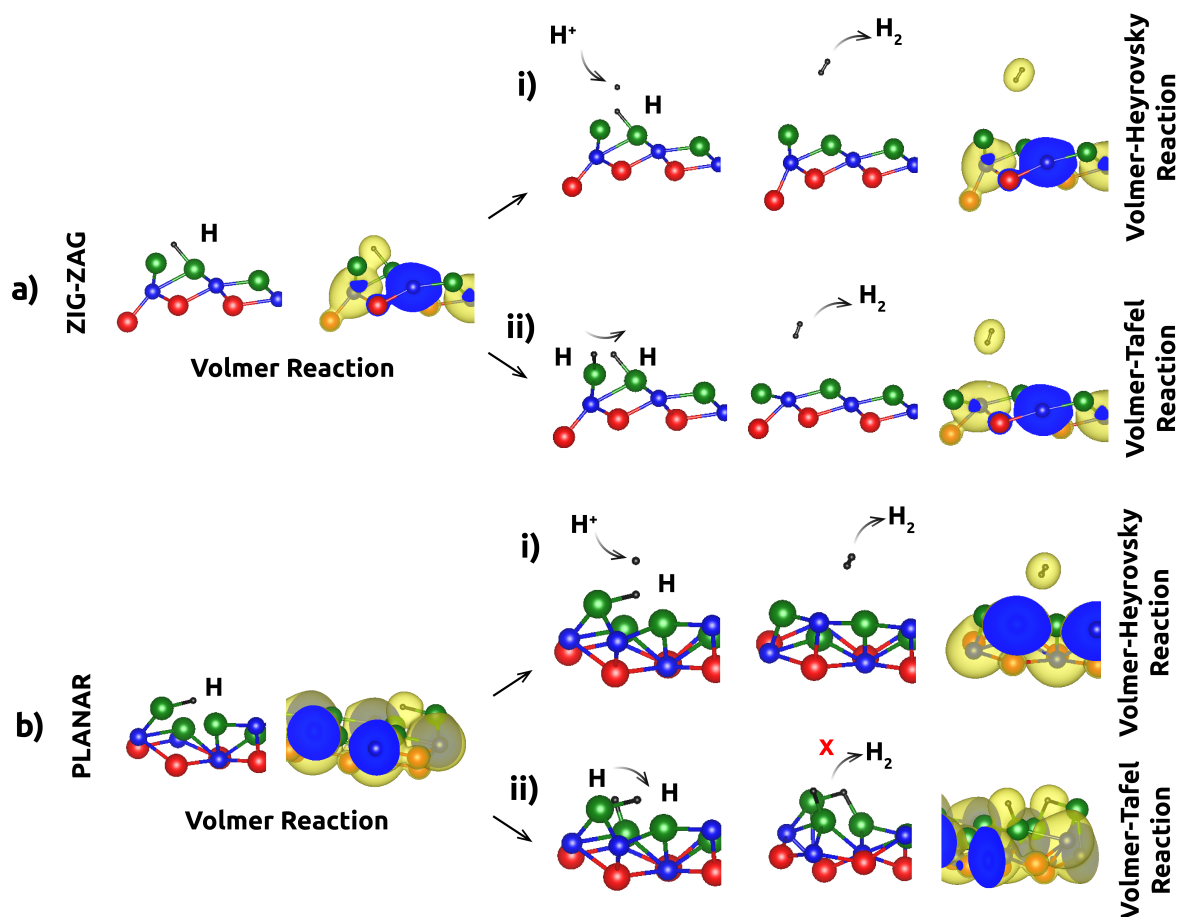


Figure 5.10: Hydrogen evolution reaction mechanism involving primary and secondary reactions at the edge sites of, (a) zig-zag and (b) planar nanoribbon configurations.

spin-orbit interactions (with spin-orbit interactions) were, As (As and Li-As) and As (As, Li) respectively. We observed close to ideal adsorption and Gibbs free energy (in zig-zag configuration with spin-orbit interaction) of, -0.264 eV and -0.024 eV at As top site and, -0.26 eV and -0.02 eV at Li-As bridge site respectively (values for other sites are tabulated in Tab. 5.2). We found that, similar to the zig-zag configurations, planar configurations also exhibit close to ideal adsorption and Gibbs free energy (under spin-orbit interactions) of, -0.213 eV and 0.026 eV at Li top site and, -0.212 eV and 0.027 eV at As top site respectively (values for other sites are tabulated in Tab. 5.3). We further confirmed and associated the origin of such excellent catalytic activity to the topological edge states by computing the primary reaction at the mid sites of nanoribbon, especially on top of those sites where the Gibbs free energy was minimum under spin-orbit interactions (along the edges). We found that, in both nanoribbon configurations, zig-zag and planar, the interactions at the mid site were of repelling nature with adsorption energy and Gibbs free energy of, 0.118 eV and 0.679 eV and, 0.358 eV and 0.919 eV respectively. Hence, we firmly establish the fact that, the

5. Energy Applications of Bulk and Low Dimensional Topological Materials

superior catalytic behaviour indeed originates from the topologically robust edge sites.

Spin-orbit interaction	Site	E_H^{ads} (eV)	ΔG_H (eV)
OFF	Li	-1.016	-0.776
	Mg	-0.301	-0.060
	As	-0.202	0.037
	Li-As	-0.948	-0.708
	Mg-As	-0.959	-0.719
ON	Li	-0.021	0.218
	Mg	-0.057	0.182
	As	-0.264	-0.024
	Li-As	-0.260	-0.020
	Mg-As	-0.278	-0.038
	Mid-As	0.118	0.358

Table 5.2: Adsorption and Gibbs free energy at different sites of zig-zag nanoribbon configuration.

Spin-orbit interaction	Site	E_H^{ads} (eV)	ΔG_H (eV)
OFF	Li	-0.281	-0.041
	Mg	0.078	0.318
	As	-0.282	-0.042
	Li-As	0.045	0.285
	Mg-As	-0.269	-0.029
ON	Li	-0.213	0.026
	Mg	0.189	0.429
	As	-0.212	0.027
	Li-As	0.111	0.351
	Mg-As	-0.202	0.037
	Mid-Li	0.679	0.919

Table 5.3: Adsorption and Gibbs free energy at different sites of planar nanoribbon configuration.

With excellent catalytic activity during the primary reaction, we computed secondary reaction mechanisms i.e., Volmer-Heyrovsky (the H adsorbed in primary reaction interacts with a H^+ ion and evolves into H_2) and Volmer-Tafel (the H adsorbed in primary reaction interacts with a neighbouring H and evolves into H_2) along the optimal sites observed in the zig-zag and planar nanoribbon configurations (as presented in Fig. 5.10a(i,ii) and b(i,ii)) respectively. The modified versions of adsorption and Gibbs free energy for Volmer-Heyrovsky intermediate reaction is given as, $\Delta E_{H^*}^{ads}(n) = (\frac{1}{n} E_{LiMgAs+nH^*} - E_{LiMgAs} - \frac{n}{2} E_{H_2})$ and $\Delta G_{H^*}(n) = \Delta E_{H^*}^{ads}(n) + \Delta_{ZPE} - T\Delta S$ respectively where $n = 2$ and terms having their

usual meaning.⁸⁶ Similar to the computations in case of AuI, for Volmer-Tafel intermediate reactions, we followed the modified formalism proposed by Lee et.al.

We found that, the zig-zag nanoribbon configuration facilitates both the secondary reactions Volmer-Heyrovsky and, Volmer-Tafel (as evident from Fig. 5.10a(i,ii)) with adsorption and Gibbs free energy of, -0.201 eV and 0.03 eV and, -0.296 eV and -0.05 eV respectively. Looking at the Gibbs free energy, it is clear that, the Volmer-Heyrovsky and Volmer-Tafel reaction mechanisms are exothermic and endothermic in nature respectively. Contrary to the zig-zag nanoribbon configurations, the planar nanoribbon configuration only facilitates Volmer-Heyrovsky reaction along the optimal sites As and Li (as evident from Fig. 5.10b(i,ii)) with adsorption and Gibbs free energy of, -0.53 eV and -0.29 eV respectively. This clearly established that, the zig-zag nanoribbon configuration is highly sensitive towards hydrogen evolution reaction as compared to the planar nanoribbon configuration. However, the overall conclusion is that, the non-trivial conducting edge sites of two dimensional topological insulator LiMgAs favour hydrogen evolution reaction rather than insulating basal sites.

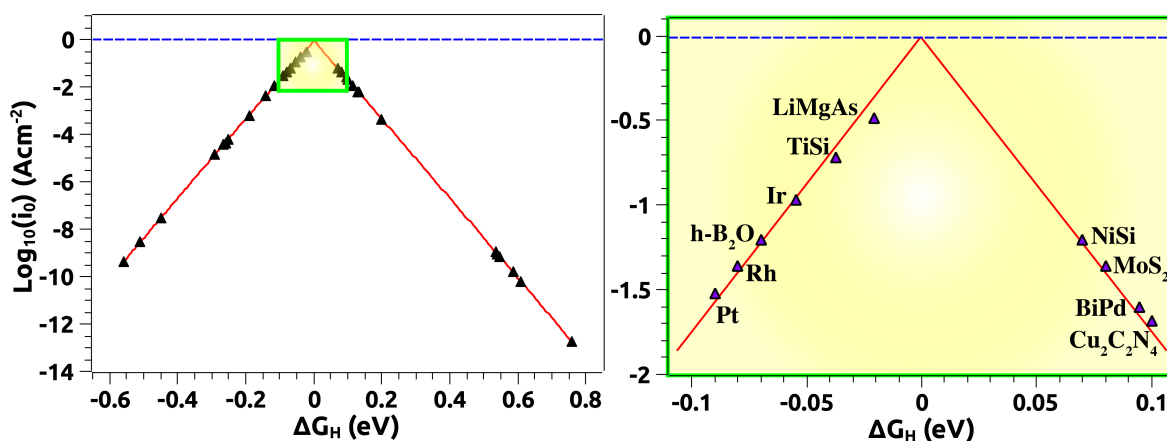


Figure 5.11: Volcano plot using, exchange current densities (for rate constant $k_0 = 1 \text{ s}^{-1} \text{ site}^{-1}$, according to Nørskov's assumptions) and Gibbs free energy data from literature for various materials. It is evident that, LiMgAs outperforms other topological materials placing it in Sabatiers optimum (highlighted in yellow).

We recomputed the exchange current densities (using, $i_0 = -ek_0 \frac{1}{1+\exp(-\frac{\Delta G_{H^*}}{k_B T})}$ for $\Delta G_{H^*} < 0$ and $i_0 = -ek_0 \frac{1}{1+\exp(\frac{\Delta G_{H^*}}{k_B T})}$ for $\Delta G_{H^*} > 0$) for various materials (using the Gibbs free energy from literature) under Nørskov's approximations with rate constant $k_0 = 1 \text{ s}^{-1} \text{ site}^{-1}$ (presented in Tab. 5.4).^{55,87-98} As compared to these materials, due to the non-trivial quantum phenomena, two dimensional topological insulator LiMgAs is placed at the top of volcano plot in a Sabatier's optimum owing to superior catalytic activity towards hydrogen evolution reaction

5. Energy Applications of Bulk and Low Dimensional Topological Materials

Material	ΔG_H (eV)	$\text{Log}_{10}(i_0)$ (Acm^{-2})	Material	ΔG_H (eV)	$\text{Log}_{10}(i_0)$ (Acm^{-2})
Pt	-0.090	-1.522	Rh	-0.080	-1.360
Pd/SnTe	-0.140	-2.349	Ni	-0.250	-4.192
<i>h</i> -B ₂ O	-0.070	-1.201	W	-0.510	-8.551
NiSi	0.070	-1.201	Co	-0.260	-4.359
MoS ₂	0.080	-1.360	Cu	0.200	-3.353
TiSi	-0.0375	-0.720	Mo	-0.450	-7.545
BiPd	0.095	-1.603	Re	-0.265	-4.443
Ni-doped-VAl ₃	0.115	-1.933	Nb	-0.560	-9.390
W/PdGa	0.200	-3.353	Au(111)	0.540	-9.054
Mo(110)	-0.290	-4.862	Ag(111)	0.545	-9.138
Mo(100)	-0.190	-3.186	PtGa	0.131	-2.199
Al(111)	0.535	-8.970	PtAl	0.132	-2.216
Al(100)	0.610	-10.228	Cu ₂ C ₂ N ₄	0.100	-1.685
LiMgAs^{present}	-0.020	-0.500	Cu(111)	0.585	-9.809
Pd	-0.115	-1.933	Ag(100)	0.760	-12.743
Ir	-0.055	-0.971			

Table 5.4: Gibbs free energy and exchange current density for various materials.

(as evident from Fig. 5.11). Such high exchange current densities (i.e., $\text{Log}_{10}(i_0) = -0.5$ Acm^{-2}) arise due to the Gibbs free energy of -0.02 eV. Apart from this, the positive Gibbs free energy at some edge sites indicates that, these sites would thermodynamically favour and readily facilitates hydrogen evolution reaction. Hence establishing the fact that two dimensional topological insulator LiMgAs is indeed a *novel* topological quantum catalyst.

5.4 Conclusion

We presented our computational results wherein, topological insulators were explored for potential energy applications such as, thermoelectrics and catalysis. We presented our computations of thermoelectric transport properties for bulk AuI due to the dense states across the Fermi level and the semi-metallic band dispersion. Due to semi-metallic nature, the electronic mobility was found to be high resulting in a high power factor. Also, we observed strong phonon-phonon scattering which lead to smaller lattice thermal conductivity. We employed the semi-classical Boltzmann transport equations to compute the thermoelectric transport coefficients. We explored the thermoelectric parameters at various temperatures and carrier concentrations. We found that, contrary to several thermoelectric materials which exhibit high figure of merit at higher temperatures, AuI exhibits excellent figure of merit of 0.55 at room temperature which is more useful from practical purposes.

We also presented our investigations on the catalytic activity of AuI monolayer towards

hydrogen evolution reaction. The dimensionally engineered AuI monolayer exposes the basal plane containing Au which is a transition metal known for superior catalytic activities. We therefore presented the hydrogen evolution reactions along the basal plane of the two dimensional topological insulator AuI. The basal plane was preferred over the edge sites because, under pristine conditions (i.e., without any strain) the non-trivial gap was found to be 14.4 meV which is far less than the thermal energy at room temperature. Hence, the edge conducting states won't be prominent which implied that, there won't be significant difference in the catalytic response of the basal plane as compared to the edge plane. We presented various mechanisms by which a hydrogen evolution reaction could occur on the basal plane of two dimensional topological insulator AuI. Based on the adsorption energy and Gibb's free energy values, we conclude that, the basal plane of AuI favours Volmer-Heyrovsky over Volmer-Tafel reaction. Also, the preferred site of interaction would be over Au rather than I since at I the hydrogen atom interacts too strongly. We confirm the evolution of hydrogen molecule by plotting the charge density profiles in 3D.

Similarly, inspired by the latest developments in the field of topological quantum catalysis, we explored two dimensional LiMgAs for topological catalysis favouring hydrogen evolution reaction. We presented the transformation of the hexagonal unit cell into an orthorhombic unit cell by using a rotation transformation matrix. The stability of the proposed system was confirmed by computing ab-initio molecular dynamics simulations. We reiterated the, non-trivial topological quantum phase transitions by presenting the exchange of charge density profiles of bands near the Fermi level. Also, we presented the electronic slab band structure which indicated the edge Dirac semi-metallic nature. This was confirmed by plotting the edge charge densities in for the zig-zag and planar-like nanoribbon configurations wherein, we observed distinct edge charge accumulations. We begin with the computation of catalytic activity on the basal plane of LiMgAs monolayer and found that the system would be inefficient due to large adsorption energies and Gibb's free energy. However, we observed that, the catalytic activity along the edges was excellent with Gibb's free energy as low as -0.02 eV. This places two dimensional topological insulator LiMgAs into the Sabartiers optimum i.e., near the top of the volcano plot with high exchange current densities. Also, we explored various mechanisms of hydrogen evolution reactions such as, Volmer, Volmer-Tafel and Volmer-Heyrovsky. Off the planar and zig-zag nanoribbon terminations, we found that, the zig-zag nanoribbon configuration facilitated both the mechanisms of hydrogen evolution reaction

5. Energy Applications of Bulk and Low Dimensional Topological Materials

(i.e., Volmer-Tafel and Volmer-Heyrovsky) whereas, the planar-like nanoribbon configuration facilitates only Volmer-Heyrovsky reaction. In order to confirm that, such superior catalytic activity is originating from the conducting edge states (due to the topological insulating nature of LiMgAs), we investigated the catalytic activity along the middle regions of the nanoribbon. We found that, the superior catalytic activity is indeed originating due to the conducting edge states and that the results are not a numerical artifact.

≈ ≈ * ≈ ≈

Bibliography

- [1] Hermann Osterhage, Johannes Gooth, Bacel Hamdou, Paul Gwozdz, Robert Zierold, and Kornelius Nielsch. *Applied Physics Letters*, 105(12):123117, 2014.
- [2] Ryuji Takahashi and Shuichi Murakami. *Semiconductor Science and Technology*, 27(12):124005, 2012.
- [3] Lukas Muchler, Frederick Casper, Binghai Yan, Stanislav Chadov, and Claudia Felser. *physica status solidi (RRL)–Rapid Research Letters*, 7(1-2):91–100, 2013.
- [4] Yuri V Ivanov, Alexander T Burkov, and Dmitry A Pshenay-Severin. *physica status solidi (b)*, 255(7):1800020, 2018.
- [5] Koushik Pal, Shashwat Anand, and Umesh V Waghmare. *Journal of Materials Chemistry C*, 3(46):12130–12139, 2015.
- [6] San-Dong Guo and Liang Qiu. *Journal of Physics D: Applied Physics*, 50(1):015101, 2016.
- [7] Ning Xu, Yong Xu, and Jia Zhu. *npj Quantum Materials*, 2(1):1–9, 2017.
- [8] Mitra Narimani, Shahram Yalameha, and Zahra Nourbakhsh. *Journal of Physics: Condensed Matter*, 32(25):255501, 2020.
- [9] Hardev S Saini, Narender Kumar, Satyender Singhmar, Jyoti Thakur, Sunita Srivastava, Manish K Kashyap, Ali H Reshak, et al. *Physics Letters A*, 384(31):126789, 2020.
- [10] Yu Zhou, Wang-Li Tao, Zhao-Yi Zeng, Xiang-Rong Chen, and Qi-Feng Chen. *Journal of Applied Physics*, 125(4):045107, 2019.

- [11] Albina Nikolaeva, Leonid Konopko, I Gherghishan, Krzysztof Rogacki, Piotr Stachowiak, Andrzej Jezowski, Vasily Shepelevich, Valerii Prokoshin, and Sofia Gusakova. *Semiconductors*, 53(5):657–661, 2019.
- [12] Min Hong, Zhi-Gang Chen, Yanzhong Pei, Lei Yang, and Jin Zou. *Physical Review B*, 94(16):161201, 2016.
- [13] Ian T Witting, Thomas C Chasapis, Francesco Ricci, Matthew Peters, Nicholas A Heinz, Geoffroy Hautier, and G Jeffrey Snyder. *Advanced Electronic Materials*, 5(6):1800904, 2019.
- [14] Jun Tang, Rui Xu, Jian Zhang, Di Li, Weiping Zhou, Xiaotong Li, Zhihe Wang, Feng Xu, Guodong Tang, and Guang Chen. *ACS applied materials & interfaces*, 11(17):15543–15551, 2019.
- [15] Tiantian Jia, Jesus Carrete, Zhenzhen Feng, Shuping Guo, Yongsheng Zhang, and Georg KH Madsen. *Physical Review B*, 102(12):125204, 2020.
- [16] Carlos A Polanco and Lucas Lindsay. *Physical Review B*, 97(1):014303, 2018.
- [17] Yunshan Zhao, Dan Liu, Jie Chen, Liyan Zhu, Alex Belianinov, Olga S Ovchinnikova, Raymond R Unocic, Matthew J Burch, Songkil Kim, Hanfang Hao, et al. *Nature communications*, 8(1):1–8, 2017.
- [18] Taneli Juntunen, Tomi Koskinen, Vladislav Khayrudinov, Tuomas Haggren, Hua Jiang, Harri Lipsanen, and Ilkka Tittonen. *Nanoscale*, 11(43):20507–20513, 2019.
- [19] Zhao Li, Sha Huang, Yufan Liu, Bin Yao, Tian Hu, Haigang Shi, Jiangfan Xie, and Xiaobing Fu. *Scientific reports*, 8(1):1–8, 2018.
- [20] Qi Chen and Gregory A Fiete. *Physical Review B*, 93(15):155125, 2016.
- [21] Bitan Roy and S Das Sarma. *Physical Review B*, 90(24):241112, 2014.
- [22] R Amarnath, KS Bhargavi, and SS Kubakaddi. *Journal of Physics: Condensed Matter*, 32(22):225704, 2020.
- [23] Maxime Markov, Xixiao Hu, Han-Chun Liu, Naiming Liu, S Joseph Poon, Keivan Esfarjani, and Mona Zebarjadi. *Scientific Reports*, 8(1):1–10, 2018.

-
- [24] Manisha Samanta, Koushik Pal, Umesh V Waghmare, and Kanishka Biswas. *Angewandte Chemie International Edition*, 59(12):4822–4829, 2020.
- [25] Maxime Markov, S Emad Rezaei, Safoura Nayeb Sadeghi, Keivan Esfarjani, and Mona Zebarjadi. *Physical Review Materials*, 3(9):095401, 2019.
- [26] Yu Zhou, Ying-Qin Zhao, Zhao-Yi Zeng, Xiang-Rong Chen, and Hua-Yun Geng. *Physical Chemistry Chemical Physics*, 21(27):15167–15176, 2019.
- [27] Rex Lundgren, Pontus Laurell, and Gregory A Fiete. *Physical Review B*, 90(16):165115, 2014.
- [28] Yupeng Shen, Fancy Qian Wang, and Qian Wang. *Nano Energy*, page 104822, 2020.
- [29] Olle Hellman and David A Broido. *Physical Review B*, 90(13):134309, 2014.
- [30] Shenghong Ju, Takuma Shiga, Lei Feng, and Junichiro Shiomi. *Physical Review B*, 97(18):184305, 2018.
- [31] Yu Xiao, Cheng Chang, Yanling Pei, Di Wu, Kunling Peng, Xiaoyuan Zhou, Shengkai Gong, Jiaqing He, Yongsheng Zhang, Zhi Zeng, et al. *Physical Review B*, 94(12):125203, 2016.
- [32] Tao Ouyang and Ming Hu. *Journal of Applied Physics*, 117(24):245101, 2015.
- [33] Peijun Guo, Yi Xia, Jue Gong, Constantinos C Stoumpos, Kyle M McCall, Grant CB Alexander, Zhiyuan Ma, Hua Zhou, David J Gosztola, John B Ketterson, et al. *ACS Energy Letters*, 2(10):2463–2469, 2017.
- [34] Jose A Alarco, Alison Chou, Peter C Talbot, and Ian DR Mackinnon. *Physical Chemistry Chemical Physics*, 16(44):24443–24456, 2014.
- [35] Yongqing Cai, Gang Zhang, and Yong-Wei Zhang. *Journal of the American Chemical Society*, 136(17):6269–6275, 2014.
- [36] Ting-Han Chou, Lucas Lindsay, Alexei A Maznev, Jateen S Gandhi, Donna W Stokes, Rebecca L Forrest, Abdelhak Bensaoula, Keith A Nelson, and Chi-Kuang Sun. *Physical Review B*, 100(9):094302, 2019.

- [37] Eric Osei-Agyemang, Challen Enninful Adu, and Ganesh Balasubramanian. *npj Computational Materials*, 5(1):1–7, 2019.
- [38] Saikat Mukhopadhyay, Lucas Lindsay, and David J Singh. *Scientific Reports*, 6:37076, 2016.
- [39] Zhe Cheng, Virginia D Wheeler, Tingyu Bai, Jingjing Shi, Marko J Tadjer, Tatyana Feygelson, Karl D Hobart, Mark S Goorsky, and Samuel Graham. *Applied Physics Letters*, 116(6):062105, 2020.
- [40] G At Slack. *Journal of Physics and Chemistry of Solids*, 34(2):321–335, 1973.
- [41] Dingfeng Yang, Wei Yao, Yanci Yan, Wujie Qiu, Lijie Guo, Xu Lu, Ctirad Uher, Xiaodong Han, Guoyu Wang, Tao Yang, et al. *NPG Asia Materials*, 9(6):e387–e387, 2017.
- [42] Chao Yuan, Jiahan Li, Lucas Lindsay, David Cherns, James W Pomeroy, Song Liu, James H Edgar, and Martin Kuball. *Communications Physics*, 2(1):1–8, 2019.
- [43] Yan-Ling Pei, Jiaqing He, Jing-Feng Li, Fu Li, Qijun Liu, Wei Pan, Celine Barreateau, David Berardan, Nita Dragoie, and Li-Dong Zhao. *NPG Asia Materials*, 5(5):e47, 2013.
- [44] Xingyong Huang, Luo Yan, Yong Zhou, You Wang, Hai-Zhi Song, and Liujiang Zhou. *The Journal of Physical Chemistry Letters*, 12(1):525–531, 2020.
- [45] Pooja Kapoor, Arun Kumar, Munish Sharma, Jagdish Kumar, Ashok Kumar, and PK Ahluwalia. *Materials Science and Engineering: B*, 228:84–90, 2018.
- [46] S Rodríguez-Barrero, J Fernández-Larrinoa, I Azkona, LN López de Lacalle, and R Polvorosa. *Materials and Manufacturing Processes*, 31(5):593–602, 2016.
- [47] Ann F Marshall, Irene A Goldthorpe, Hemant Adhikari, Makoto Koto, Young-Chung Wang, Lianfeng Fu, Eva Olsson, and Paul C McIntyre. *Nano letters*, 10(9):3302–3306, 2010.
- [48] Xiao Huang, Shaozhou Li, Shixin Wu, Yizhong Huang, Freddy Boey, Chee Lip Gan, and Hua Zhang. *Advanced Materials*, 24(7):979–983, 2012.
- [49] Courtney M Payne, Dmitri E Tsentalovich, Denise N Benoit, Lindsey JE Anderson, Wenhua Guo, Vicki L Colvin, Matteo Pasquali, and Jason H Hafner. *Chemistry of Materials*, 26(6):1999–2004, 2014.

- [50] Zhanxi Fan, Michel Bosman, Xiao Huang, Ding Huang, Yi Yu, Khuong P Ong, Yuriy A Akimov, Lin Wu, Bing Li, Jumiati Wu, et al. *Nature communications*, 6(1):1–8, 2015.
- [51] Yoshifumi Oshima, Akiko Onga, and Kunio Takayanagi. *Physical review letters*, 91(20):205503, 2003.
- [52] Robbie Burch. *Physical Chemistry Chemical Physics*, 8(47):5483–5500, 2006.
- [53] Tokuhisa Kawawaki and Yuichi Negishi. *Nanomaterials*, 10(2):238, 2020.
- [54] Tatyana Tabakova. *Frontiers in chemistry*, 7:517, 2019.
- [55] Jens Kehlet Nørskov, Thomas Bligaard, Ashildur Logadottir, JR Kitchin, Jingguang G Chen, S Pandelov, and U Stimming. *Journal of The Electrochemical Society*, 152(3):J23, 2005.
- [56] Paola Quaino, Fernanda Juarez, Elizabeth Santos, and Wolfgang Schmickler. *Beilstein journal of nanotechnology*, 5(1):846–854, 2014.
- [57] Fengwang Li and Mianqi Xue. *TWO-DIMENSIONAL MATERIALS*, page 63, 2016.
- [58] Narayan N Som and Prafulla K Jha. *International Journal of Hydrogen Energy*, 45(44):23920–23927, 2020.
- [59] Shan Wang, Aolin Lu, and Chuan-Jian Zhong. *Nano Convergence*, 8(1):1–23, 2021.
- [60] Shasha Li, Enze Li, Xiaowei An, Xiaogang Hao, Zhongqing Jiang, and Guoqing Guan. *Nanoscale*, 13:12788–12817, 2021.
- [61] J Peng, W Dong, Z Wang, Y Meng, W Liu, P Song, and Z Liu. *Materials today advances*, 8:100081, 2020.
- [62] Chongyi Ling, Yixin Ouyang, Li Shi, Shijun Yuan, Qian Chen, and Jinlan Wang. *ACS Catalysis*, 7(8):5097–5102, 2017.
- [63] Charlie Tsai, Frank Abild-Pedersen, and Jens K Nørskov. *Nano letters*, 14(3):1381– 1387, 2014.
- [64] Thomas R Hellstern, Jakob Kibsgaard, Charlie Tsai, David W Palm, Laurie A King, Frank Abild-Pedersen, and Thomas F Jaramillo. *ACS Catalysis*, 7(10):7126–7130, 2017.

- [65] Tien D Tran, Mai TT Nguyen, Hoang V Le, Duc N Nguyen, Quang Duc Truong, and Phong D Tran. *Chemical Communications*, 54(27):3363–3366, 2018.
- [66] Haifeng Lv, Zheng Xi, Zhengzheng Chen, Shaojun Guo, Yongsheng Yu, Wenlei Zhu, Qing Li, Xu Zhang, Mu Pan, Gang Lu, et al. *Journal of the American Chemical Society*, 137(18):5859–5862, 2015.
- [67] Wenlei Zhu, Ronald Michalsky, O?nder Metin, Haifeng Lv, Shaojun Guo, Christopher J Wright, Xiaolian Sun, Andrew A Peterson, and Shouheng Sun. *Journal of the American Chemical Society*, 135(45):16833–16836, 2013.
- [68] Guowei Li and Claudia Felser. *Applied Physics Letters*, 116(7):070501, 2020.
- [69] Qingfang Chang, Xilin Zhang, and Zongxian Yang. *Applied Surface Science*, 565:150568, 2021.
- [70] Zhe Meng, Bikun Zhang, Qiong Peng, Yadong Yu, Jian Zhou, and Zhimei Sun. *Applied Surface Science*, 562:150151, 2021.
- [71] Barack Obama. *Science*, 355(6321):126–129, 2017.
- [72] Zhi Wei Seh, Jakob Kibsgaard, Colin F Dickens, IB Chorkendorff, Jens K Nørskov, and Thomas F Jaramillo. *Science*, 355(6321):eaad4998, 2017.
- [73] Shipeng Ding, Max J Hülsey, Javier Pérez-Ramírez, and Ning Yan. *Joule*, 3(12):2897–2929, 2019.
- [74] Min Zeng and Yanguang Li. *Journal of Materials Chemistry A*, 3(29):14942–14962, 2015.
- [75] Dusan Strmcnik, Pietro Papa Lopes, Bostjan Genorio, Vojislav R Stamenkovic, and Nenad M Markovic. *Nano Energy*, 29:29–36, 2016.
- [76] Hua Chen, Wenguang Zhu, Di Xiao, and Zhenyu Zhang. *Physical review letters*, 107(5):056804, 2011.
- [77] P Sabatier. *La catalyse en chimie organique*, librairie polytechnique, 1920.
- [78] H Gerischer. *Bulletin des Sociétés Chimiques Belges*, 67(7-8):506–527, 1958.

-
- [79] Roger Parsons. *Transactions of the Faraday Society*, 54:1053–1063, 1958.
- [80] Paola Quaino, Fernanda Juarez, Elizabeth Santos, and Wolfgang Schmickler. *Beilstein journal of nanotechnology*, 5(1):846–854, 2014.
- [81] Ruikuan Xie, Tan Zhang, Hongming Weng, and Guo-Liang Chai. *Small Science*, page 2100106, 2022.
- [82] Guowei Li and Claudia Felser. *Applied Physics Letters*, 116(7):070501, 2020.
- [83] Shuo Wang, Ben-Chuan Lin, An-Qi Wang, Da-Peng Yu, and Zhi-Min Liao. *Advances in Physics: X*, 2(3):518–544, 2017.
- [84] Subramaniam Jayabal, Jian Wu, Jiaye Chen, Dongsheng Geng, and Xiangbo Meng. *Materials today energy*, 10:264–279, 2018.
- [85] Aidi Zhao and Bing Wang. *APL Materials*, 8(3):030701, 2020.
- [86] Chi Ho Lee, Byeongsun Jun, and Sang Uck Lee. *RSC advances*, 7(43):27033–27039, 2017.
- [87] Pengtang Wang, Xu Zhang, Jin Zhang, Sheng Wan, Shaojun Guo, Gang Lu, Jianlin Yao, and Xiaoqing Huang. *Nature communications*, 8(1):1–9, 2017.
- [88] Qing Qu, Bin Liu, Wing Sum Lau, Ding Pan, and Iam Keong Sou. *arXiv preprint arXiv:2112.04753*, 2021.
- [89] Xiaofeng Zhao, Xiaoyong Yang, Deobrat Singh, Pritam Kumar Panda, Wei Luo, Yuxiang Li, and Rajeev Ahuja. *The Journal of Physical Chemistry C*, 124(14):7884–7892, 2020.
- [90] Wei Liu, Xiaoming Zhang, Weizhen Meng, Ying Liu, Xuefang Dai, and Guodong Liu. *Iscience*, 25(1):103543, 2022.
- [91] Berit Hinnemann, Poul Georg Moses, Jacob Bonde, Kristina P Jørgensen, Jane H Nielsen, Sebastian Horch, Ib Chorkendorff, and Jens K Nørskov. *Journal of the American Chemical Society*, 127(15):5308–5309, 2005.
- [92] Jiangxu Li, Hui Ma, Qing Xie, Shaobo Feng, Sami Ullah, Ronghan Li, Junhua Dong, Dianzhong Li, Yiyi Li, and Xing-Qiu Chen. *Science China Materials*, 61(1):23–29, 2018.

- [93] Yuan He, Dong Yan, Li Ren Ng, Lei Shi, Shu Wang, Hsin Lin, Shi-Hsin Lin, Huixia Luo, and Kai Yan. *Materials Chemistry Frontiers*, 3(10):2184–2189, 2019.
- [94] Xiang-Peng Kong, Tao Jiang, JiaoJiao Gao, Xianbiao Shi, Jian Shao, Yunhuan Yuan, Hua-Jun Qiu, and WeiWei Zhao. *The Journal of Physical Chemistry Letters*, 12(15):3740–3748, 2021.
- [95] Qun Yang, Guowei Li, Yudi Zhang, Jian Liu, Jiancun Rao, Thomas Heine, Claudia Felser, and Yan Sun. *npj Computational Materials*, 7(1):1–8, 2021.
- [96] Joakim Ekspong, Eduardo Gracia-Espino, and Thomas Wagberg. *The Journal of Physical Chemistry C*, 124(38):20911–20921, 2020.
- [97] Qun Yang, Guowei Li, Kaustuv Manna, Fengren Fan, Claudia Felser, and Yan Sun. *Advanced Materials*, 32(14):1908518, 2020.
- [98] Lirong Wang, Xiaoming Zhang, Weizhen Meng, Ying Liu, Xuefang Dai, and Guodong Liu. *Journal of Materials Chemistry A*, 9(39):22453–22461, 2021.

